Dynamic model of target charging by short laser pulse interactions

A. Poyé,[1] J.-L. Dubois,[1] F. Lubrano-Lavaderci,[2] E. D'Humières,[1] M. Bardon,[2] S. Hulin,[1] M. Bailly-Grandvaux,[1] J. Ribolzi,[2] D. Raffestin,[2] J. J. Santos,[1] Ph. Nicolaï,[1] and V. Tikhonchuk[1]

[1]*Centre Lasers Intenses et Applications, University of Bordeaux, CNRS, CEA, Talence 33405, France*

[2]*CEA/DAM/CESTA, BP 12, Le Barp 33405, France*

(Received 17 July 2015; published 21 October 2015; corrected 29 October 2015)

A model providing an accurate estimate of the charge accumulation on the surface of a metallic target irradiated by a high-intensity laser pulse of fs–ps duration is proposed. The model is confirmed by detailed comparisons with specially designed experiments. Such a model is useful for understanding the electromagnetic pulse emission and the quasistatic magnetic field generation in laser-plasma interaction experiments.

DOI: 10.1103/PhysRevE.92.043107 PACS number(s): 52.38.Kd, 41.20.Gz, 41.75.Jv

I. INTRODUCTION

Recent developments of high-power laser sources raise the acute problem of electromagnetic pulse generation in laser-target interactions. On one side, these electromagnetic pulses can be very harmful for diagnostic equipment at distances of a few meters from the source. On another side, it can be an attractive way to produce intense quasistatic magnetic fields with various applications.

The electromagnetic pulse created during the interaction of an intense subpicosecond laser pulse with a solid target contains two spectral components [1–3]. The first one is related to the current of fast electrons ejected from the target and corresponds to an electromagnetic emission in the THz domain [4]. Although the amplitude of such a current could be rather high, the pulse duration is too short and electronic circuits are not sensitive in this spectral domain [5]. The second one is due to the neutralization current flowing through the target holder. It is much longer, of the nanosecond time scale, corresponding to the GHz spectral domain. Depending on the target-holder system, this neutralization current can be oscillating, generating a so-called electromagnetic pulse (EMP), which propagates into the interaction chamber [6] and may be harmful for electronic devices. The neutralization current can also be aperiodic and used for new applications related to directed electromagnetic pulses and for production of strong quasistatic magnetic fields [7,8].

Experimental demonstration of the dominant role of the neutralization current in the EMP generation together with a simple analytical model and large-scale numerical simulations has been published recently [6,9]. But detailed numerical simulations of the target charging process require large-scale simulations with hydrodynamic, Monte Carlo, and particle-in-cell codes [6], which do not allow a systematic investigation of the EMP dependence with the experiment parameters. We propose here a simplified quasianalytical model permitting a rapid evaluation of the target charge in function of the target and laser parameters. It allows us to identify the relevant effects in this multiphysics process of laser-matter interaction and to predict the EMP characteristics. The analysis reveals different charging regimes depending on the laser and target parameters. The paper is organized as follows. Section II presents a qualitative description of the target charging physics. The following sections give the model details and the associated evolution equations: the electrons cloud in Sec. III and the potential barrier in Sec. IV. Section V contains comparison with experiments and discussions of specific cases. The Appendices A, B, C, and D gather the calculation details of some parts of the model. The model is accompanied with a FORTRAN90 program (ChoCoLaT.f90) calculating the charging current and the final charge for a given set of input parameters. The practical details of the numerical equations solver and instructions for users are presented in Appendix E.

II. GLOBAL DESCRIPTION

Interaction of intense short laser pulses with solid targets results in a strong electron acceleration and heating. Some of these hot electrons are ejected from the target, while others spread and dissipate their energy inside of it. We assume the target to be thick enough compared to the range of electron propagation. Schematically, one may imagine a cylindrical cloud of hot electrons with radius and height R_h, a temperature T_h, full of N_h electrons, centered on the laser focal spot, and expanding with time, see Fig. 1. A fraction of the electrons is traveling out the target front face to a distance of the order of their Debye length λ_{Dh}. They are creating a sheath potential ϕ_{th} at this target front surface, retaining a majority of electrons inside. Only the most energetic ones can escape this potential barrier and leave the target definitely. These escaping energetic electrons constitute the electric current J_h charging positively the target. Moreover, these escaped electrons are at the origin of another (dipolar) contribution to the potential barrier, ϕ_E. It corresponds to the net positive charge distributed over the target surface. Thus, the global potential barrier can be evaluated by adding these two potentials $\Phi = \phi_E + \phi_{\mathrm{th}}$. This description illustrates the coupling of different elements of the problem: the hot electron cloud, the potential barrier at the target surface, and the ejection current J_h.

For modeling those phenomena, we are considering space-averaged hot electron characteristics and writing down simple evolution equations for them. The major simplifying assumptions are described by a Maxwell-Jütner energy distribution function. It is expressed as:

$$f_h(\varepsilon, T_h) = \frac{\gamma\, p}{\mathcal{A}} \exp(-\varepsilon / k_B T_h), \tag{1}$$

where p is the electron momentum, γ is the relativistic factor, and ε is the energy, see Fig. 2. This figure also illustrates the fraction of electrons which can possibly escape from the target:

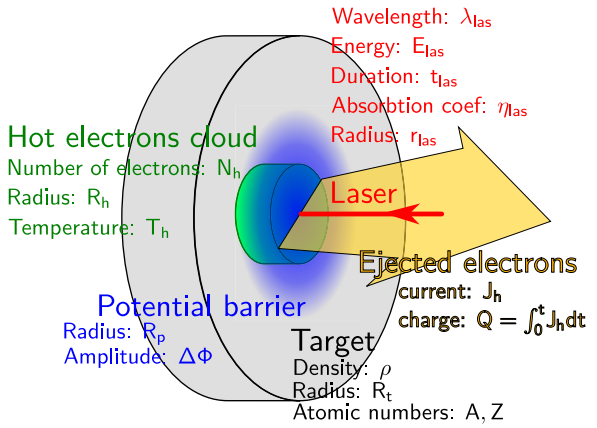

FIG. 1. (Color online) Scheme of target charging by laser and the key interaction parameters.

$\varepsilon \geqslant e\Delta\Phi$, with $\Delta\Phi$ the potential barrier defined in Sec. IV. The normalization factor $\mathcal{A}$ in the distribution function (1) is defined as $1 = \int_0^\infty f_h d\varepsilon$. The use of such a distribution for the hot electrons is justified by a fast collisional relaxation of laser-heated electrons in the solid target at low energy.

The laser parameters are E_{las} (the energy), t_{las} [the duration, full width at half maximum (FWHM)], λ_{las} (the wavelength), η_{las} (the energy absorption coefficient), and r_{las} [the focal radius, half width at half maximum (HWHM)]. The temporal and spatial profiles of the laser pulse are assumed to be Gaussian functions. The dimensionless laser vector potential is $a_{las} = 0.85\lambda_{las} I_{las}^{1/2}$ and the laser intensity is $I_{las} = 0.65 E_{las}/(t_{las}\pi r_{las}^2)$ in the units of 10^{18} W cm^{-2} [10].

The model requires the temperature of electrons accelerated by the laser. Various scaling laws have been proposed for this initial temperature and for the laser absorption coefficient. Those issues are still creating controversy because of a large variation of the interaction conditions and laser pulse characteristics. We do not want to enter into such details, which are out of the scope of this paper. Thus, we consider here the laser absorption coefficient η_{las} as a free parameter, which is reported in the existent literature to vary in the range

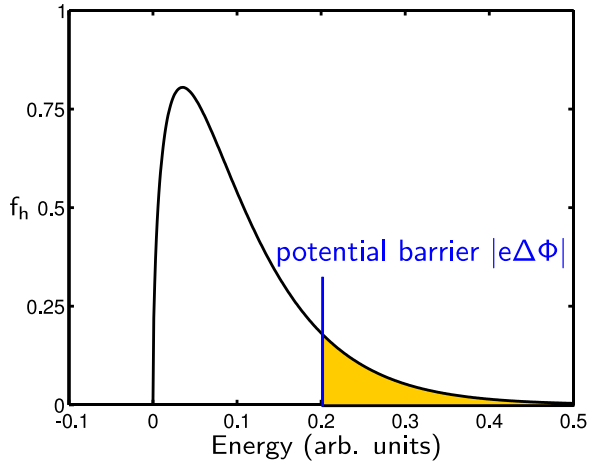

FIG. 2. (Color online) Maxwell-Juttner distribution function and the potential barrier Φ.

between 10 and 50% (fixed at 40% for this article, except when specified). As for the initial hot electron temperature we choose Beg's empirical law [11] in the interval $0.03 \lesssim a_{las} \lesssim 1$ and the ponderomotive scaling [12] for higher laser intensities:

$$T_0 = m_e c^2 \max\left\{0.47\, a_{las}^{2/3},\quad \sqrt{1 + a_{las}^2} - 1\right\}. \tag{2}$$

For the intensities below 10^{15} W cm^{-2} ($a_{las} \lesssim 0.03$), the temperature is estimated from the model of laser collisional absorption [13], $T_0 = 3 m_e c^2 a_{las}^{4/3}$. These expressions agree with the experimental data within a factor of 2 [10].

We introduce also three averages over the distribution function:

$$\langle\cdot\rangle = \int_0^\infty f_h(\varepsilon, T_h) d\varepsilon, \tag{3a}$$

$$\langle\cdot\rangle_0 = \int_0^\infty f_h(\varepsilon, T_0) d\varepsilon, \tag{3b}$$

$$\langle\cdot\rangle_{hot} = \frac{1}{\mathcal{A}_{hot}} \int_{|e\Delta\Phi|}^\infty f_h(\varepsilon, T_h) d\varepsilon, \tag{3c}$$

with $\mathcal{A}_{hot} = \int_{|e\Delta\Phi|}^\infty f_h d\varepsilon$ being a fraction of electrons that may escape the target. The simple brackets (3a) define the average over the whole distribution function (1). The subscript "0" (3b) stands for the initial temperature T_0 in the distribution function. The bracket with subscript "hot" (3c) defines the average over the escaped electrons only, with an energy larger than $|e\Delta\Phi|$.

We summarize here the various notations used in the article. The laser parameters have the subscript "las." The subscript "0" stands for the initial value of the variable. The subscript "h" defines the hot electron variable during its evolution. The subscript "hot" defines the average over the escaped electrons only, with an energy higher than $|e\Delta\Phi|$.

III. THREE EFFECTS THAT MODIFY THE HOT ELECTRON CLOUD

The dynamics of the hot electron cloud is due to three major processes discussed in the following four subsections: in Sec. III A the laser heating, in Sec. III B the hot-cold electron collision cooling, and in Sec. III C the hot electron ejection from the target. The product of the cloud temperature and the number of electrons in the cloud gives the total energy of the cloud W_h. Those three effects modify W_h by changing N_h and/or T_h. Then the cloud parameters that we monitor are the temperature T_h and the electrons number N_h. In Sec. III D we describe the evolution of the cloud radius R_h.

A. Laser heating

The laser heating creates the hot electrons, following the Maxwell-Juttner energy distribution function at a temperature T_0. We assume a linear production of hot electrons within the time of laser energy injection t_{las}. The total number of hot electrons is noted N_{tot} and is the ratio between the laser energy and the initial hot electron average energy:

$$N_{tot} = \frac{\eta_{las} E_{las}}{\langle\varepsilon\rangle_0}. \tag{4}$$

The hot electron production rate is estimate as:

$$\partial_t N_h = \frac{N_{\rm tot}}{t_{\rm las}} \text{ if } \quad t < t_{\rm las}. \tag{5}$$

The laser injects $N_{\rm tot}$ electrons at an energy $\langle\varepsilon\rangle_0$ during $t_{\rm las}$. Due to the energy conservation, we assume that the hot electron average energy and temperature are constant during the injection period.

To summarize, the laser heating increases the number of hot electrons and sustains their temperature during the laser pulse time.

B. Hot electron collisional cooling

The hot-cold electrons collisions are responsible for the energy transfer from the hot electrons to the bulk electrons. The characteristic collision time is defined by the electron diffusion length divided by the thermal speed. It is averaged over electron energy distribution so we define t_{ee} as the mean free flight time, see Appendix A. The collisional cooling proceeds in three temporal steps. The first is for $t_{\rm las}$, when we assume that the temperature is constant. However, collisions with cold electrons imply a reduction of the number of hot electrons from the cloud. This is particularly important for $t_{ee} \ll t_{\rm las}$ where some hot electrons disappear from the cloud even before the laser pulse ends. It results in a loss term with the characteristic time $t_{\rm life}$ which is the mean free flight time plus a cooling time, defined in Appendix A:

$$\partial_t N_h = -N_h/t_{\rm life} \quad \text{if} \quad t < t_{\rm las}. \tag{6}$$

The second effect is the hot electron temperature reduction. There are two cases. First, during the laser pulse and before the first collision there is no cooling. After that time, the collisions linearly reduce the hot electron temperature with the characteristic time t_{ee}. Then the electron temperature equation reads:

$$\partial_t T_h = -T_h/t_{ee} \quad \text{if} \quad t > t_{\rm las} + t_{ee}. \tag{7}$$

The collisional cooling can also be seen as a reduction of the hot electron energy W_h. For $t < t_{\rm las}$, the cloud loses electrons of the energy $\langle\varepsilon\rangle_0$ but for $t > t_{\rm las}$, it is the mean energy $\langle\varepsilon\rangle$ of hot electrons which is reduced and not the number of electrons.

C. Hot electron ejection

The hot electrons with an energy higher than the potential barrier $|e\Delta\Phi|$ can escape from the cloud if they propagate in the correct direction. Assuming an ejection cone of half-angle β, we consider that a fraction $\Omega_\beta = (1-\cos\beta)/2$ of electrons has the appropriate direction for ejection, see Appendix A. We define the current J_h as the flux of the electrons which have enough energy to escape the potential. It is defined later in Eq. (18c). Considering the ejection surface πR_h^2, the hot electron current reads:

$$J_h = e\,\Omega_\beta\, n_{\rm hot}\,\pi R_h^2 \int_{|e\Delta\Phi|}^{\infty} f_h v\, d\varepsilon, \tag{8}$$

where e is the elementary charge and v is the electron speed.

The ejection of the most energetic electrons modifies the electron distribution by reducing its energy and the number of electrons. The reduction of the number of hot electrons in the cloud is defined by the ejection current:

$$\partial_t N_h = -J_h/e. \tag{9}$$

The energy loss is related to the temperature evolution. We assume that the temperature is proportional to the averaged energy of the electrons: $T_h \propto \langle\varepsilon\rangle = W_h/N_h$. Then the variation of the total hot electron energy W_h reads: $\partial_t W_h = -J_h\langle\varepsilon\rangle_{\rm hot}/e$. Combining this equation with Eq. (9) we obtain:

$$\partial_t\langle\varepsilon\rangle = -\frac{\langle\varepsilon\rangle J_h}{N_h e}\left(1 - \frac{\langle\varepsilon\rangle_{\rm hot}}{\langle\varepsilon\rangle}\right). \tag{10}$$

With the assumed proportionality between $\langle\varepsilon\rangle$ and T_h, we obtain an expression for the temperature ejection loss:

$$\partial_t T_h = -\frac{T_h J_h}{N_h e}\left(1 - \frac{\langle\varepsilon\rangle_{\rm hot}}{\langle\varepsilon\rangle}\right). \tag{11}$$

Furthermore, the ejection is limited not by the number of electrons in the cloud but by the number of electrons, which have enough energy to escape. This condition imposes a limit on the ejected charge, which takes two forms, whether it is applied during or after the laser pulse. During the laser pulse, we assume that the ejection current cannot be larger than the amount of ejectable electrons created by the laser:

$$I_{h,\max} = e\frac{\eta_{\rm las} E_{\rm las}\mathcal{A}_{\rm hot}}{t_{\rm las}\langle\varepsilon\rangle_0} \text{ if } \quad t < t_{\rm las}. \tag{12}$$

After the laser pulse, the collision cooling does not affect the number of hot electrons. Then we define a maximal number of electrons, which is ejectable from the cloud. The maximal charge ejectable is then the charge ejected during the laser pulse plus the maximal remaining charge:

$$Q(t > t_{\rm las})_{\max} = Q(t_{\rm las}) + eN_h(t_{\rm las})\mathcal{A}_{\rm hot}. \tag{13}$$

If this maximum is reached, then the ejection current is stopped.

D. Cloud radius description

The cloud radius R_h is related to the electron mean free path. We assume that the hot-cold electron collisions damp the hot electron energy, whereas the collision of a hot electron with an ion only affects its propagation direction and not its energy. The characteristic hot electron-ion collision time t_{ei} is given in Appendix A. The radius evolution depends on the average electron speed, which is not related to the cloud temperature T_h. Indeed, the cloud expands from the very beginning of the laser pulse. As these electrons propagate out of the laser focal spot they are losing their energy and the cloud expansion is slowed down. However, we already assumed that the cloud temperature T_h is sustained by the laser, while the energy of electron defining the cloud radius is decreasing.

If $t_{\rm las} \ll t_{ee}$, then this difference between the electrons in the laser spot and the cloud periphery is negligible as all hot electrons are created instantly compared to the cooling time. But in the opposite case, $t_{\rm las} \gg t_{ee}$, the thermal electron speed would be nonphysically sustained on a time greater than its own cooling time. In order to circumvent this controversy, which is due to model simplifications, we introduce a local temperature Θ_h, without laser sustainment, which represents

the mean energy of the first electron created by the laser. Here the thermal speed and the diffusion time t_{ee} are calculated with the distribution function $f_h(\varepsilon,\Theta_h)$, Eq. (1). For the sake of simplicity, the Θ_h evolution accounts only for the hot-cold electron collision term with the initial condition $\Theta_0 = T_0$. The initial value of the hot electron cloud radius is equal to the focal spot radius $R_0 = r_{\rm las}$.

Then we obtain the following equations for the radius evolution:

$$\partial_t \Theta_h = 0 \quad \text{if } t < t_{ee}, \tag{14a}$$

$$\partial_t \Theta_h = -\Theta_h / t_{ee} \quad \text{if } t_{ee} < t, \tag{14b}$$

$$\partial_t R_h = \langle v \rangle \quad \text{if } t < t_{ei}, \tag{15a}$$

$$\partial_t R_h = \frac{\langle v \rangle^2 t_{ei}}{2R_h} \quad \text{if } t_{ei} < t. \tag{15b}$$

Note that with those equations, it is the cloud radius which is sustained by the laser and no longer the thermal speed.

E. Hot electron evolution equations

We summarize here the full set of equations describing the evolution of the hot electron cloud. They contain three main effects explained before. The equation for the number of electrons in the cloud, with $N_0 = 0$ as the initial value:

$$\partial_t N_h = \frac{N_{\rm tot}}{t_{\rm las}} - \frac{N_h}{t_{\rm life}} - \frac{J_h}{e} \quad \text{if } t < t_{\rm las}, \tag{16a}$$

$$\partial_t N_h = -\frac{J_h}{e} \quad \text{if } t > t_{\rm las}. \tag{16b}$$

The equation for the cloud temperature with T_0 as the initial value:

$$\partial_t T_h = 0 \quad \text{if } t < t_{\rm las}, \tag{17a}$$

$$\partial_t T_h = \frac{J_h T_h}{e N_h}\left(1 - \frac{\langle \varepsilon \rangle_{\rm hot}}{\langle \varepsilon \rangle}\right) \quad \text{if } t_{\rm las} < t < t_{ee} + t_{\rm las}, \tag{17b}$$

$$\partial_t T_h = \frac{J_h T_h}{e N_h}\left(1 - \frac{\langle \varepsilon \rangle_{\rm hot}}{\langle \varepsilon \rangle}\right) - \frac{T_h}{t_{ee}} \quad \text{if } t > t_{ee} + t_{\rm las}. \tag{17c}$$

These equations are completed with the following expressions for the cloud volume and density:

$$V_h = \pi R_h^2 (R_h - r_{\rm las}), \tag{18a}$$

$$n_h = \frac{N_h}{V_h}, \tag{18b}$$

$$n_{\rm hot} = \frac{N_h \mathcal{A}_{\rm hot}}{V_h}. \tag{18c}$$

IV. POTENTIAL DESCRIPTION

A. Thermal potential

The thermal potential is generated by the charge separation at the target surface [14–16]. Consequently, one needs to model the charge separation first and then to compute the associated potential. As the accelerated electrons can move in every direction, some of them move out of the target but are repelled back by the potential $\phi_{\rm th}$ associated with the space charge. The electron space charge is described by the Poisson equation, Eq. (19), assuming the Boltzmann distribution of electrons in the potential:

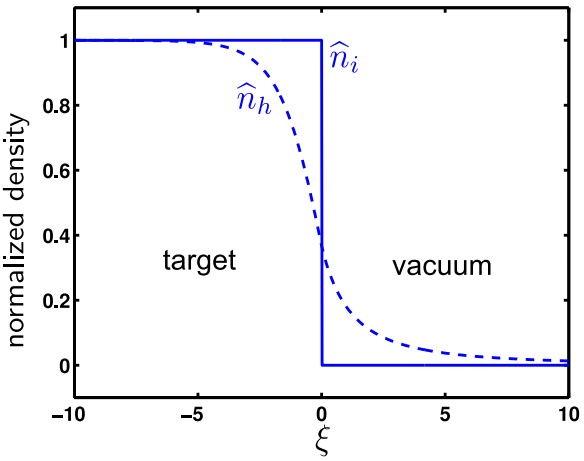

FIG. 3. (Color online) Density profiles for ions (full line) and electrons (dashed line) near the target edge.

$$\epsilon_0 \nabla^2 \phi_{\rm th} = -e[n_i - n_h \exp(e\phi_{\rm th}/k_B T_h)], \tag{19}$$

where ϵ_0 is the vacuum dielectric permittivity. The ion density is described by a Heaviside function, $n_i = n_h \mathcal{H}(\xi)$, where the coordinate $\xi = 0$ defines the target surface. This hypothesis is valid as long as the ion density scale length is smaller than the hot electron Debye length defined below. We focus on the laser axis direction: It is the escaping direction for the hot electrons.

The problem is intricated by the fact that Eq. (19) has a divergent solution for the potential in one dimension [17]. Therefore formally no electron can escape the target. However, the pure one-dimensional (1D) model fails on distances larger than the electron cloud radius. A relatively simple approximate solution can be found assuming that the electron cloud radius is larger than the hot electron Debye length. As the electron density is a converging function in the 1D model, see Fig. 3, we apply it in three dimensions assuming that it is localized within the radius $r < R_h$. The 1D electron density distribution reads:

$$n_e(r < R_h, \xi) = \frac{N_h}{V_h}\begin{cases} 1 + [\exp(-1) - 1]\exp(\kappa\xi/\lambda_{\rm Dh}) & \xi < 0, \\ [\exp(1/2) + \xi/\lambda_{\rm Dh}\sqrt{2}]^{-2} & \xi > 0, \end{cases} \tag{20}$$

where $\lambda_{\rm Dh}$ is the hot electron Debye length and $\kappa = (\exp(1) - 1)/\sqrt{2\exp(1)}$. The derivation of this expression is discussed in Appendix B.

The potential $\phi_{\rm th}$ is then estimated from a three-dimensional calculation with the electric charge density given by Eq. (20):

$$\phi_{\rm th}(x,r) = \frac{e}{4\pi\epsilon_0}\int_{-\infty}^{\infty}\int_0^{R_h}\int_0^{2\pi} \frac{[n_i(\xi) - n_e(\xi)]\, d\xi\, \rho\, d\rho\, d\theta}{\sqrt{(x-\xi)^2 + r^2 + \rho^2 - \rho r\cos\theta}}. \tag{21}$$

The system coordinates and an example of $\phi_{\rm th}$ reconstruction are presented in Fig. 4. It is important to note here that

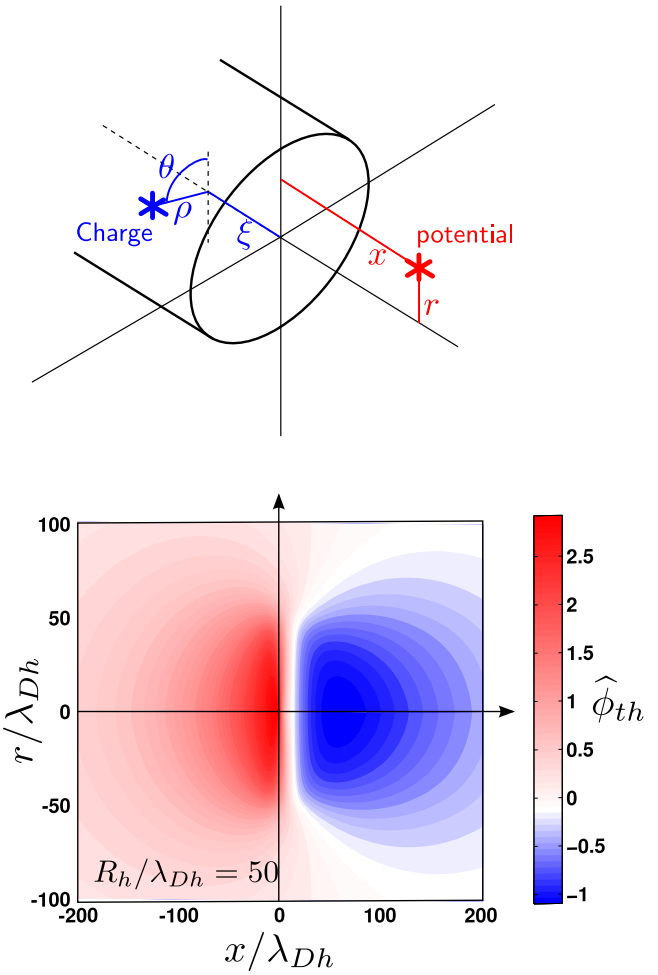

FIG. 4. (Color online) (top) Three-dimensional geometry of the potential numerical reconstruction and (bottom) the map of potential for $R_h/\lambda_{\mathrm{Dh}} = 50$, negative values for $x/\lambda_{Dh} > 0$ and positive values for $x/\lambda_{Dh} < 0$.

the potential normalized to the hot electron temperature, $\widehat{\phi}_{\mathrm{th}} = e\phi_{\mathrm{th}}/k_B T_h$, depends only on the normalized radius $\widehat{R} = R_h/\lambda_{\mathrm{Dh}}$. This is a universal function which can be tabulated or analytically interpolated. Once the potential $\widehat{\phi}_{\mathrm{th}}(r,x)$ is calculated, we define the thermal part of the barrier as a difference between the minimum and maximum ϕ_{th} values averaged over the cylinder section.

The normalized potential along the laser axis can also be evaluated analytically. Details are provided in Appendix C. The analytical expression reads:

$$\tilde{\phi}_{\mathrm{th}}(z) = \frac{\lambda + z}{\sqrt{(z+\lambda)^2+1}} \times \ln\left[\frac{\sqrt{(z+\lambda)^2+1}\sqrt{z^2+1}+1+z(z+\lambda)}{(\sqrt{(z+\lambda)^2+1}-z-\lambda)\lambda}\right] - \sinh^{-1}(z) - \ln 2 + \begin{cases} -\ln(\lambda) & \text{if} \quad z < 0 \\ -2\ln(\lambda+z)+\ln(\lambda) & \text{if} \quad z > 0 \end{cases} \tag{22}$$

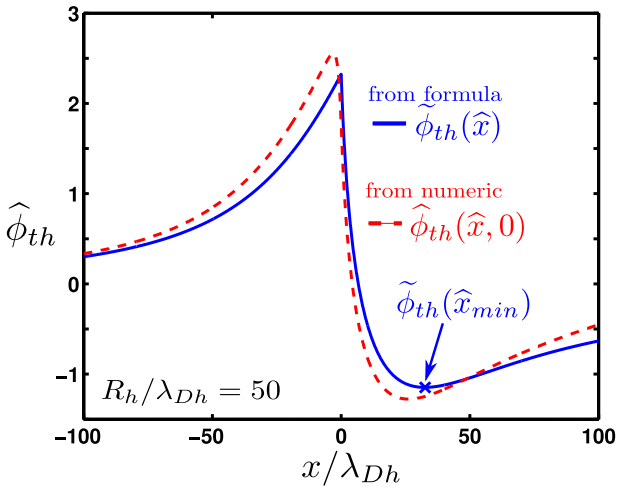

FIG. 5. (Color online) Comparison of the potential $\widehat{\phi}_{\mathrm{th}}$ from the analytical calculation or from the numerical reconstruction.

with $\lambda = \sqrt{2e}\lambda_{\mathrm{Dh}}/R_h$ and $z = x/R_h$. Figures 5 and 6 shows a comparison between the potential found from the numerical reconstruction and from the analytical calculation. The potential ϕ_{th} reaches its maximum at the target edge $z = 0$. Inside

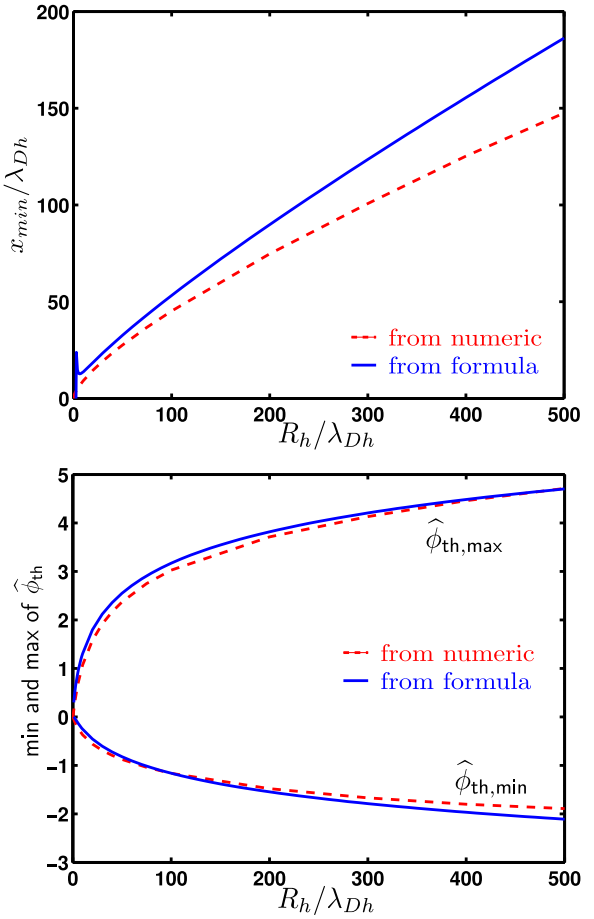

FIG. 6. (Color online) (bottom) Comparison of the minimum and the maximum of the thermal potential and (top) the minimum position of the thermal potential. Data from the analytical calculation or from the numerical reconstruction.

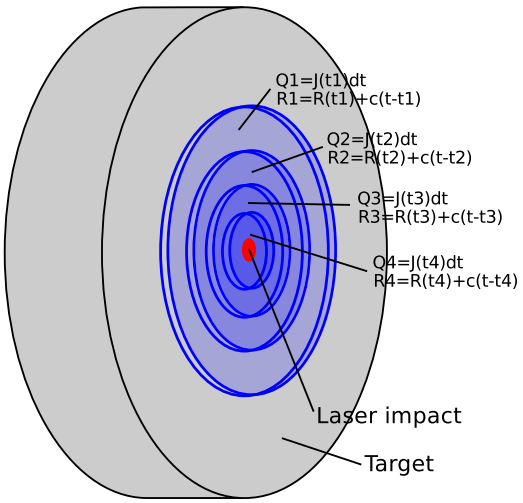

FIG. 7. (Color online) Scheme of four successive charged disks at a time t, which were born at four arbitrary times $t_1 < t_2 < t_3 < t_4 < t$.

the target the potential is positive approaching the asymptotic value $\phi_{\rm th}(-\infty) = 0$. Outside the target the potential sign switches and reaches its minimum value $\widetilde{\phi}_{\rm th\,min}$ at the position $z_{\rm min} \simeq -2/\ln\lambda$. Then it approaches the asymptotic value $\phi_{\rm th}(\infty) = 0$.

Knowing the precalculated function $\widehat{\phi}_{\rm th}$ and accounting for the normalization, one obtains the potential $\phi_{\rm th}$ as a function of T_h, n_h, R_h and implicitly of the time t.

B. Electrostatic potential

The electrostatic potential is created by the positive charge at the surface of the target left by the current of ejected hot electrons. We consider it as a surface charge homogeneously distributed over a disk of a radius R_p. At each time step dt', a new positive charge $J_h(t')dt'$ is appearing at the target. If the target material is a conductor, this surface charge spreads over the whole the target surface at the speed of light c,

$$R_p(t',t) = R_h(t') + c\,(t - t') \text{ with } 0 < t' < t. \qquad (23)$$

Then the elementary potential distribution along the disk axis reads:

$$d\phi_E(t',t,x) = \frac{J_h(t')\left[\sqrt{R_p^2(t',t) + x^2} - |x|\right]}{2\epsilon_0\pi\, R_p^2(t',t)} dt'.$$

For conducting targets, the total electrostatic potential can be represented as a superposition of homogeneously charged elementary disks in expansion. This is represented schematically in Fig. 7. The total electrostatic potential ϕ_E is then defined as follows:

$$\phi_E(t,x) = \int_0^t dt' \frac{J_h(t')\left[\sqrt{R_p^2(t',t) + x^2} - |x|\right]}{2\epsilon_0\pi\, R_p^2(t',t)}. \qquad (24)$$

It is positive everywhere and decreases to zero at infinity, $|x| \to \infty$.

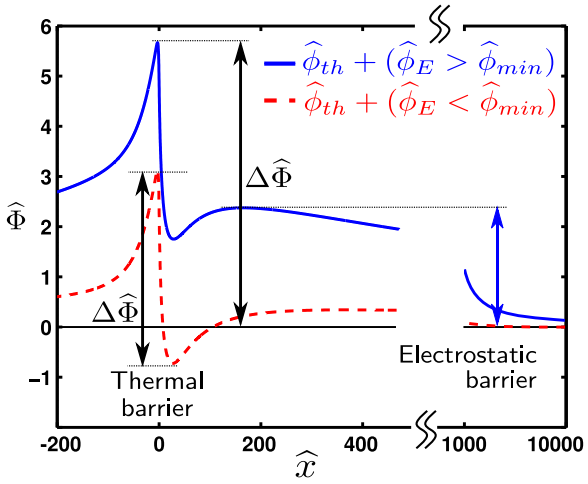

FIG. 8. (Color online) Two examples of the total potential $\Phi = \phi_{\rm th} + \phi_E$, and the effective potential barrier $\Delta\Phi$.

C. Determination of the potential barrier

Knowing both potentials, ϕ_E and $\phi_{\rm th}$, one can determine the potential barrier for escaping electrons $\Delta\Phi$. It is defined as a difference between the maximum and the minimum of the potential Φ as a function of the axial coordinate x for a given radial position. The potential maximum is located at or close to the target surface where both potentials have a positive sign. Asymptotically, both potentials tend towards zero at $|x| \to \infty$. As concerning the potential minimum, two situations can occur: Either the total potential is positive everywhere, and then the maximum value of the potential defines the height of the potential barrier, or the thermal potential dominates, and the total potential switches sign and the height of the potential barrier is defined by the difference between the potential maximum and minimum. Both situations are shown in Fig. 8. If $|\phi_{\rm th} = (t,x_{\rm min})| < \phi_E(t,x_{\rm min})$, then the minimum at the position $x_{\rm min}$ is local and the minimum of the whole potential is 0 at $|x| = \infty$. If $|\phi_{\rm th}(t,x_{\rm min})| > \phi_E(t,x_{\rm min})$, then the minimum is $\phi_E(t,x_{\rm min}) + \phi_{\rm th}(t,x_{\rm min})$. These two cases are cast into the formula:

$$\Delta\Phi(t) = \phi_E(t,0) + \phi_{\rm th}(t,0) - \min\{\phi_E(t,x_{\rm min}) + \phi_{\rm th}(t,x_{\rm min}),0\}. \qquad (25)$$

V. RESULTS AND DISCUSSIONS

A. Comparison with experimental results

The model described in the previous section is realized as numerical program written as a FORTRAN90 script. It can be compiled and executed on a PC. The numerical details are presented in Appendix E. Here we present a comparison of the model with an experiment performed on the laser ECLIPSE [6,9]. The laser pulse was focused on a solid flat disk of 1 cm diameter and 3 mm thickness. Several materials have been tested: aluminum, copper, and tantalum. The charge left on the target was measured by integrating the neutralization current through the target holder with a fast oscilloscope.

Figure 9 shows in each panel the charge measured in the experiment and that predicted by the model for all the metallic

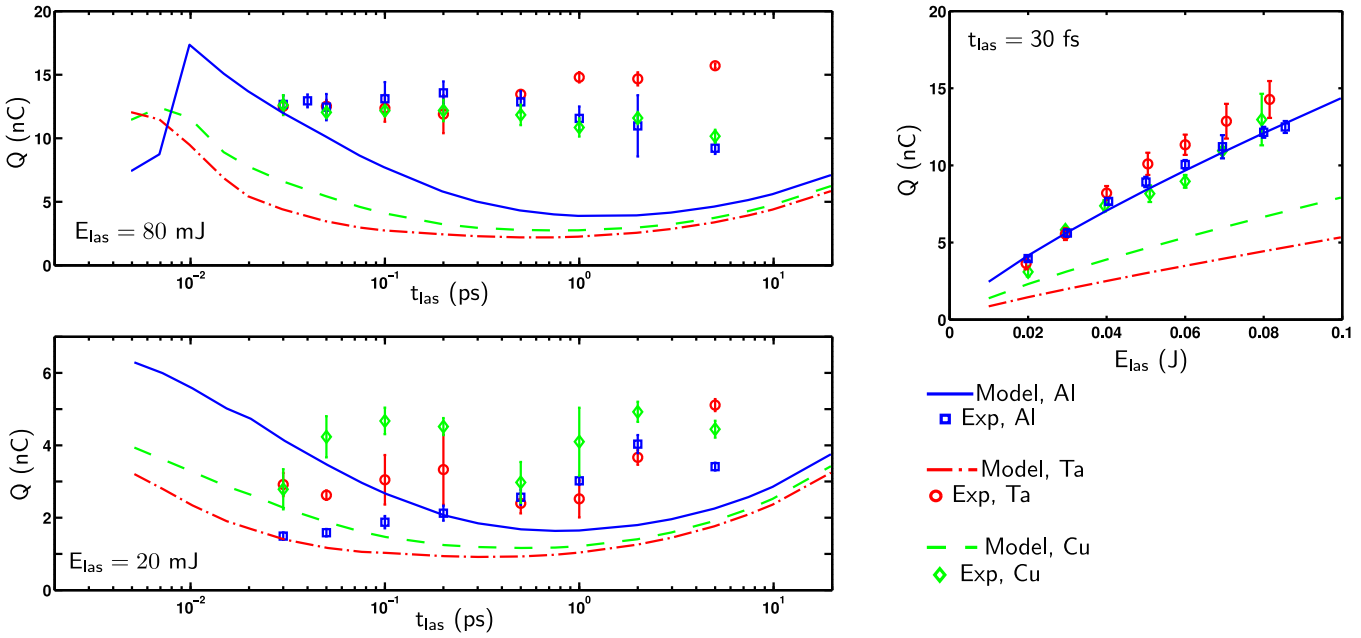

FIG. 9. (Color online) Experimental measurements of the charge (symbols) and the model predictions (curves) for scans on the laser energy and on the laser pulse duration: $E_{las} = 20$ to 80 mJ, $t_{las} = 30$ fs to 5 ps, $\lambda_{las} = 800$ nm, $r_{las} = 6\,\mu$m, and $\eta_{las} = 40\%$.

targets. The overall agreement with the model is reasonable. In the worst cases, the difference does not exceed a factor of 3. This is acceptable keeping in mind the voluntary simplicity of the model, which aims at qualitative understanding of the charging phenomenon and at calculating the charge estimate.

We can define three different ejection regimes: (i) the steady-state ejection regime corresponds to laser pulses longer than the cooling time; (ii) the full ejection regime corresponds to very short and intense laser pulses where the hot electrons have, in average, an energy greater than the potential barrier; and (iii) the thermal ejection regime is intermediate between the two previous limits. The limits of those regimes are presented in Fig. 10 where t_{ee} is compared to t_{las} and the potential barrier is compared to the hot electron energy. This comparison is performed with values averaged over the time with a charge weight function. For example, the time average of the hot electron energy is

$$\overline{\langle\varepsilon\rangle} = \frac{\int_0^{t_{las}+t_{life}} \langle\varepsilon\rangle J_h(t)dt}{Q(t_{las}+t_{life})}. \tag{26}$$

B. Three ejection regimes

1. Steady-state regime

For the pulse duration longer than the cooling time, the cloud is sustained by the laser. Indeed, in this limit, Eqs. (15), (16), and (17) are reduced to their equilibrium values. The temperature is kept constant at the initial level T_0 according to Eq. (2). The cloud radius reaches its maximum value, which can be estimated as

$$R_h \simeq r_{las} + t_{life}\langle v\rangle_0. \tag{27}$$

The number of hot electrons in the cloud is obtained by solving the steady-state Eq. (16a) neglecting the ejection current. In this regime,

$$N_h \simeq N_{tot} t_{life}/t_{las}. \tag{28}$$

As the temperature is constant and the cloud is sustained, the thermal potential is constant. The electrostatic potential reaches an equilibrium value because the ejection current contribution in Eq. (24) is compensated by the increase of the charged disk radius. Consequently, the ejection current J_h is also constant and it can be approximated if we provide an average value of the electrostatic potential. It can be found by averaging Eq. (24) over t_{las}, assuming J_h to be constant. In this

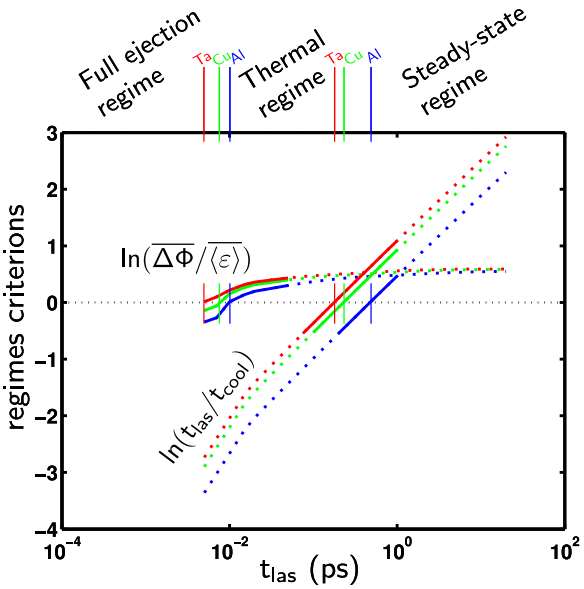

FIG. 10. (Color online) Ejection regime limits for $E_{las} = 80$ mJ, $\lambda_{las} = 800$ nm, $r_{las} = 6\,\mu$m, and $\eta_{las} = 40\%$ for the aluminum (blue), tantalum (red), and copper (green) targets. The regime limits are close for all materials as shown by the three set of curves.

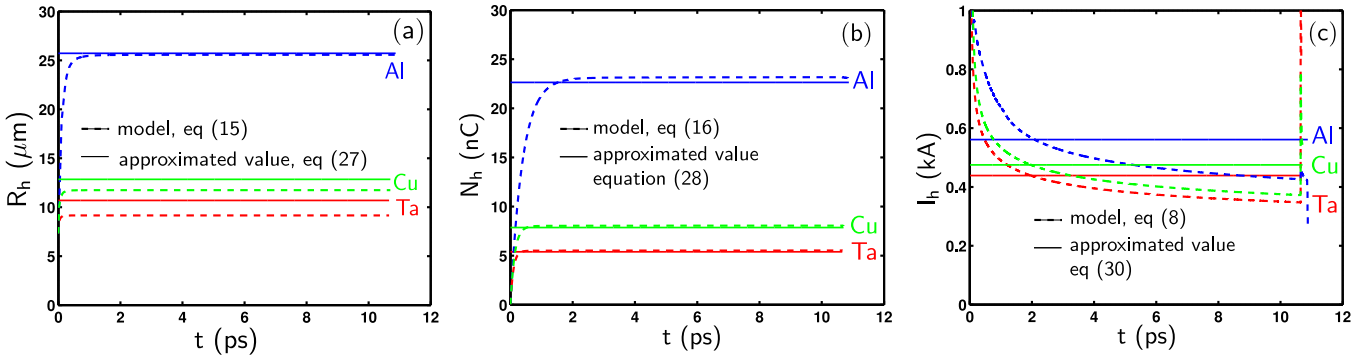

FIG. 11. (Color online) Temporal evolution of the cloud radius, R_h (a), the total number of hot electrons, N_h (b), and the ejection current, J_h (c) in the steady-state regime (dashed lines) and the comparison with their approximated values in this regime (solid lines). $t_{las} = 10$ ps, $E_{las} = 80$ mJ, $\lambda_{las} = 800$ nm, $r_{las} = 6\,\mu$m, and $\eta_{las} = 40\%$.

approximation, Eq. (23) is also simplified with the limiting value given by Eq. (27) for R_h. Indeed, the cloud radius is sustained at its maximum during the whole emission time. The average value of the potential is then obtained from Eq. (25) using the averaged electrostatic potential:

$$\phi_E(0) \simeq \frac{J_h}{2\varepsilon_0 c}\left[\left(1+\frac{R_h}{ct_{las}}\right)\ln\left(1+\frac{ct_{las}}{R_h}\right)-1\right], \quad (29a)$$

$$\phi_E(x_{min}) \simeq \phi_E(0) + \frac{J_h x_{min}}{2\varepsilon_0 c}\left[\frac{1}{ct_{las}}\ln\left(1+\frac{ct_{las}}{R_h}\right)-\frac{1}{R_h}\right]. \quad (29b)$$

One obtains for the ejection current and the target charge:

$$J_h \simeq -\Omega_\beta e \frac{N_{tot}}{t_{las}\langle v\rangle_0}\int_{|e\Delta\Phi|}^{\infty} f_h(\varepsilon,T_0) v\, d\varepsilon, \quad (30a)$$

$$Q \simeq J_h t_{las}. \quad (30b)$$

which is a simple differential equation since J_h is a function of $\Delta\Phi$. Figure 11 presents a comparison between the model and this approximation in the steady-state regime.

2. *Full ejection regime*

For very short pulse durations, the laser intensity is high as is the hot electron temperature. The first consequence is that the total number of hot electrons N_{tot} decreases. Each hot electron takes more energy, but their number is relatively smaller, according to Eq. (4). Also, the potential barrier is not high enough to keep the hot electrons inside the target. The thermal barrier is weak because the hot electron density is low, despite the high temperature. The electrostatic barrier remains low also because the number of hot electrons is small. Figure 10 already illustrates these features by a comparing the hot electron average energy with the average potential barrier. Combining these observations we define the *full ejection regime* where the electron average energy is higher than the potential barrier. The ejection time is larger than the pulse duration but shorter than the lifetime. The ejection process happens mainly during the mean collision time t_{ee} where the ejection terms dominate, as shown in Fig. 12. In this regime, a rough approximation of the target charge is simply $Q_h \approx eN_{tot}$, that is, the total number of hot electrons generated with the laser. Figure 13 shows the comparison between the model result and this approximation. The full ejection regime correspond to the laser pulse duration less than 10 fs for this set of parameters.

3. *Thermal regime*

This regime is between the two previous ones. The pulse duration is shorter than the cooling time, but the laser intensity

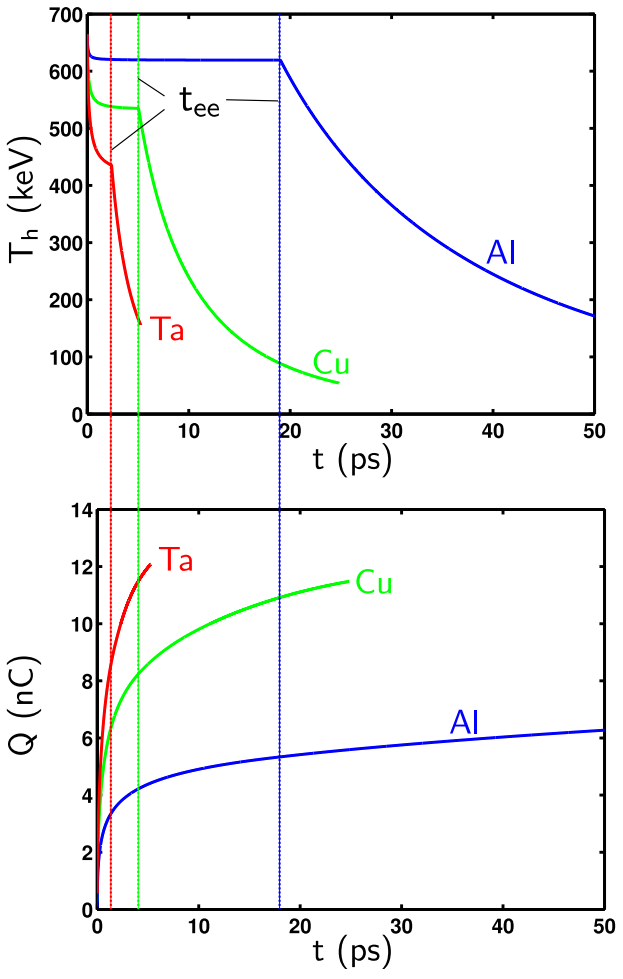

FIG. 12. (Color online) Temperature and charge evolution in the full ejection regime. The charge is already at 80% of its maximum at the time t_{ee}. $E_{las} = 0.8$ J, $t_{las} = 5$ fs, $\lambda_{las} = 800$ nm, $r_{las} = 6\,\mu$m, and $\eta_{las} = 40\%$.

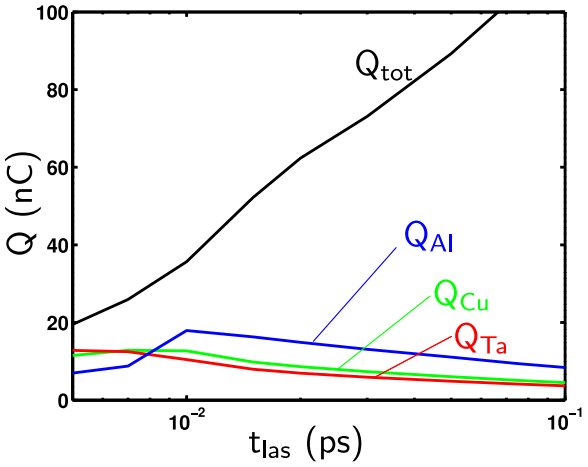

FIG. 13. (Color online) Comparison between $Q_{\rm tot}$ and the final charge obtained in the full ejection regime: $E_{\rm las} = 0.8$ J, $\lambda_{\rm las} = 800$ nm, $r_{\rm las} = 6\,\mu$m, and $\eta_{\rm las} = 40\%$.

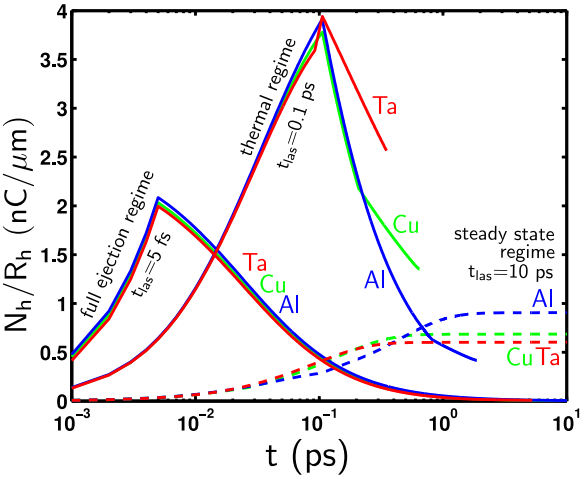

FIG. 14. (Color online) Time evolution of $N_h/(R_h - r_{\rm las})$ for three materials. The electron surface charge is material independent except a slight deviation in the thermal regime. $E_{\rm las} = 0.8$ J, $\lambda_{\rm las} = 800$ nm, $r_{\rm las} = 6\,\mu$m, and $\eta_{\rm las} = 40\%$.

is not high enough to invalidate the barrier efficiency. Physics is mainly determined by the cooling of the hot electron cloud in the target. There is no simplification available in this regime because all the model variables are evolving.

C. Charge independence on the target material

A feature of the target charge measured in our experiments is its weak dependence on the target material. Figure 9 shows a comparison of the measured charge for targets made of three metals: They show the same behavior despite different target densities and atomic numbers. According to our model, the material parameters are playing a role in defining the cooling time and thus affecting the temporal evolution of N_h, R_h, and T_h. The observed charge independence on the target material has two explanations depending on the ejection regime.

In the full ejection regime, the hot electron ejection proceeds before any collisional cooling processes. Equation (16b) for N_h so as Eq. (15a) for R_h are then independent of the target parameters. Figure 14 shows the value of the ratio $N_h/(R_h - r_{\rm las})$ present in the current equation for the full-ejection regime. This ratio is independent on the target material.

In the steady-state regime, R_h and N_h are approximately constant because the ejection proceeds during the laser pulse. Equation (16a) can be simplified as Eq. (28). The electron cloud radius can be approximated at the first order to Eq. (27). It appears then that the ratio $N_h/(R_h - r_{\rm las})$ in the ejection current expression is again independent on $t_{\rm life}$, the only target parameter present in those expressions. The ratio $N_h/(R_h - r_{\rm las})$ for this regime is presented in Fig. 14. It is also independent of the target parameters in the steady-state regime.

The material independence in the intermediate regime is less obvious. However, accounting for the continuity between the two previous regimes, we can assume it without demonstration from the model simplification. Figure 14 shows that the ratio $N_h/(R_h - r_{\rm las})$ is approximately constant in this regime and the model results in Fig. 9 tend to confirm the charge independence on the target material in this regime.

The last parameter which is material relevant is the laser absorption coefficient in Eq. (4). We arbitrary keep its value equal to 40% for all the laser parameters used in the present article. The charge model variations are only linear with the value of $\eta_{\rm las}$ but it can explain the experimental variations of the charge, in particular in Fig. 9 at $E_{\rm las} = 80$ mJ for $t_{\rm las}$ greather than 1 ps. The laser absorption calculation is out of the scope of this article, and its better evaluation may improve the results of the model.

D. Small targets

The size of the target can be compared to several characteristic lengths present in the model; from the smallest to the largest these are the hot electron Debye length $\lambda_{\rm Dh}$, the hot electron cloud radius R_h, and the electrostatic potential radius R_p. The first two dimensions involve the target thickness and are out of the scope of this article. The third one involves the target radius. If the target is sufficiently small, then the electrostatic potential propagation must be restrained to the target radius R_t. Equation (23) becomes:

$$R_p(t',t) = \min\{R_h(t') + c\,(t - t'), R_t\} \text{ with } 0 < t' < t. \quad (31)$$

Then, after R_p reaches the target boundary, the surfacic charge accumulates and the electro-static potential increases with the charge until it suppresses the current completely. Therefore, it is expected that small targets accumulate a smaller charge. In the experiment described in Ref. [6], the charge does not depend on the target size: The target is too large to demonstrate this effect, see Fig. 15(a). The authors of experiments [18,19] report on the EMP variation with the target size, which can be related to the charge variation: The targets are small enough, see Figs. 15(b) and 15(c). Our model gives the same charge tendencies with respect to the target and laser parameters as observed in the experiments.

To quantify this target size effect, we start with the simple case of a large-enough target. Indeed, if the potential redistribution time R_t/c is larger than the charge ejection time t_{ej}, then the model predicts a maximum ejected charge. The ejection time can be estimated by $t_{ej} = \max\{t_{\rm las}, t_{ee}\}$. Then, if $R_t < ct_{ej} = R_{\rm min}$, the ejected charge may be reduced. Note

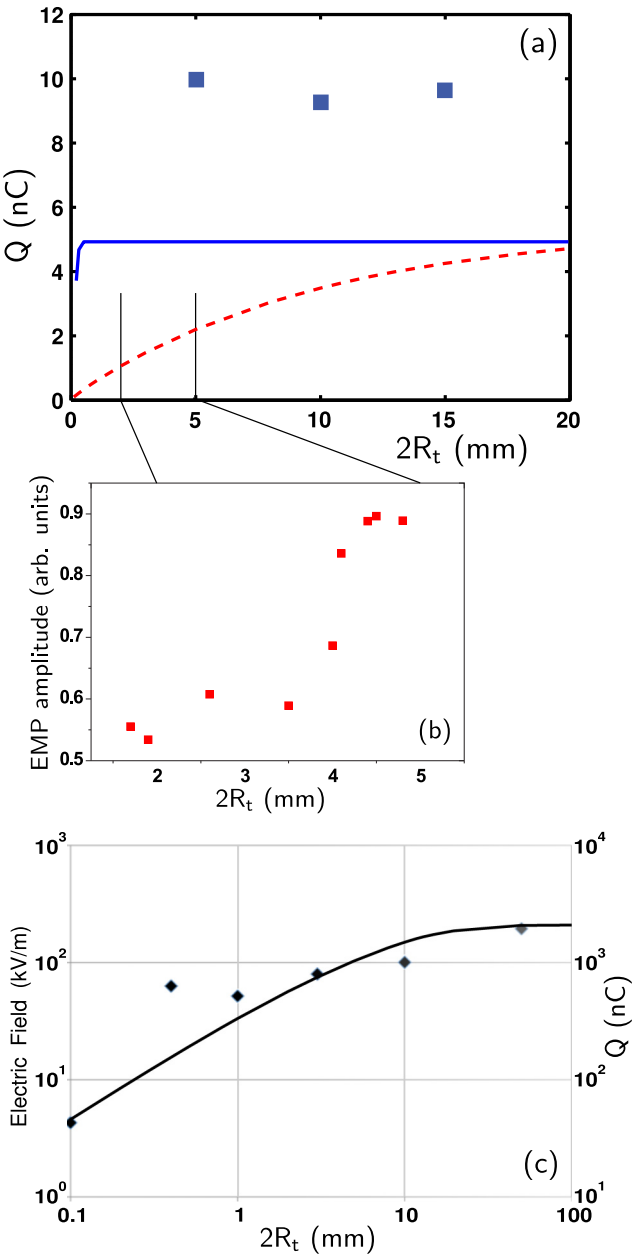

FIG. 15. (Color online) Effect of the target size on the EMP signal observed on different laser facilities. Dots are experimental measurements for the charge (a) and for the EMP electric field [(b) and (c)]. Lines are charge model predictions. (a) Top curve and dots are from ECLIPSE facility [6] ($E_{las} = 80$ mJ, $t_{las} = 50$ fs, $\lambda_{las} = 800$ nm, $r_{las} = 7.5$ μm, and $\eta_{las} = 40\%$). Bottom curve of panel (a) and the curve of panel (b) are from Ref. [19] ($E_{las} = 150$ mJ, $t_{las} = 150$ ps, $\lambda_{las} = 1064$ nm, $r_{las} = 150$ μm, and $\eta_{las} = 40\%$). (c) Data from the TITAN facility [18] ($E_{las} = 200$ J, $t_{las} = 20$ ps, $\lambda_{las} = 1050$ nm, $r_{las} = 10$ μm, and $\eta_{las} = 40\%$).

that this criterion does not account for the neutralization current, which naturally decreases the surfacic charge. We find $R_{min} = 0.5$ mm for the ECLIPSE experiment [Fig. 15(a)], $R_{min} = 30$ mm for the experiment in Ref. [19] [Figs. 15(a) and 15(b)], and $R_{min} = 20$ mm for the TITAN experiment [Fig. 15(c)]. All these estimates are consistent with the experimental observations.

Let us consider another example of a small target experiment [20], conducted at the VULCAN facility. A short laser pulse was interacting with a thin gold wire. The authors evaluated the target charge to be 48 nC. In this case, the target must be considered as a small target because its radius is small, $R_t = 125$ μm. The electrostatic potential is spreading only in one direction, which leads to the charge limitation. Using the data from Ref. [20], $E_{las} = 26$ J, $t_{las} = 1$ ps, $r_{las} = 5.6$ μm, $\eta_{las} = 20\%$, $\lambda_{las} = 1064$ nm, and $R_t = 125$ μm, we find that the target charge equals 40.4 nC, which is comparable with the measured value.

E. Dielectric targets

The use of dielectric targets is considered as a way to suppress the return current and the strength of the electromagnetic pulse. The main difference from metallic targets is in their very small conductivity. This prevents the cold electrons reorganizing to minimize the potential. This case can be included in the model with the modified calculation of the electrostatic potential. Equation (23) becomes

$$R_p(t',t) = \min\{R_h(t') + c\,(t - t'), R_h(t)\} \text{ with } 0 < t' < t. \tag{32}$$

Zero target conductivity forces the surfacic charge to accumulate in a disk limited by the hot electron cloud size. For cases with hot electron speed close to light speed, the lack of conductivity does not change significantly the charge because the hot electron cloud extension emulates the charge spread. But for cases where the hot electron speed is significantly smaller than the light speed, the restriction of the charge spread to R_h concentrates the charge and produces a higher electrostatic potential. The final charge accumulated on a dielectric target is then lower than on a metallic target.

As an illustration, Fig. 16 shows the ejected charge with a Teflon target from the model and from the ECLIPSE experiment. The target charge is approximately the same as for the metallic targets in the case of short laser pulses, see Fig. 17(a), but it decreases much faster for longer laser pulses as it is shown in Fig. 17(b). This is explained by a stronger electrostatic potential. The experimental setup is the same as in Fig. 9 and as described in Refs. [6,9]. Because of the insulation between the laser impact and the holder inserted into the target, the measurement of the neutralization current gives only a fraction of the ejected charge. A relation between the holder neutralization charge and the target charge is calculated in Appendix D and it depends strongly on the setup used. The neutralization current in the holder is always smaller with dielectric targets as for the associated EMPs. This conclusion assumes that there is no electrical breakdown between the laser impact and the holder.

F. Holder effect

Until now, we assumed that the target is connected to the ground by a conducting rod but the recharge current is activated after the charge accumulation of the target is completed. This corresponds to a holder having a large inductance, so the neutralization current is delayed enough to make an effective insulation during the target charging. Here we consider an effect of the holder on the charge accumulation assuming that

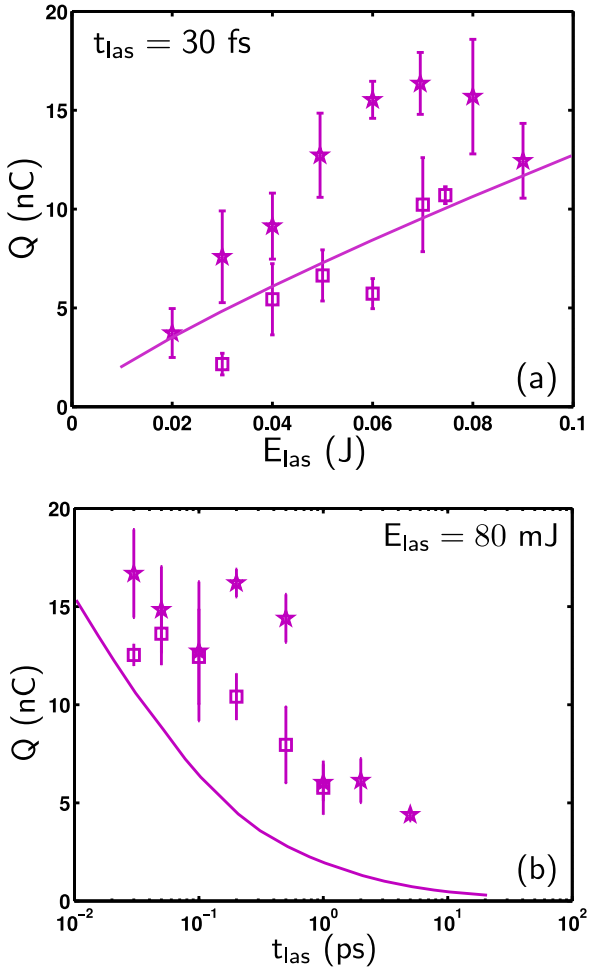

FIG. 16. (Color online) Experimental measurements of the charge and the model predictions for a scans on the laser energy and on the laser pulse duration with a Teflon target. Stars and squares are two identical targets. Lines are the model prediction. $\lambda_{las} = 800$ nm, $r_{las} = 6\ \mu$m, and $\eta_{las} = 40\%$. (a) Laser energy scan $E_{las} = 30$ to 90 mJ at $t_{las} = 30$ fs. (b) Laser pulse duration scan $t_{las} = 30$ fs to 5 ps at $E_{las} = 80$ mJ.

the neutralization current is active during the charge ejection. It can totally cancel the charge accumulation if the characteristic neutralization time t_n is much smaller than the ejection time t_{ej}.

A relation between the characteristic ejection and neutralization time defines the recharge regime. The neutralization time is roughly estimated to $t_n = L/c$: the time for a charge to travel the holder length L at the light speed. It is 150 ps for a 5-cm holder. This estimate indicates the experimental setups, which can generate strong EMP signals. Figure 17 shows the electric field measured on different laser facilities versus the laser energy. Blue points correspond to the experiments with maximal EMPs while red points corresponds to conditions, where EMPs are limited by the neutralization current. As an example: EMPs obtained on the ECLIPSE experiment with $E_{las} = 0.1$ J have the same amplitude as the ones obtained on the NIF with $E_{las} = 100$ kJ. On the ECLIPSE experiments, the ejection time is between 1 and 20 ps, while the neutralization time equals 100 ps: the target charging is maximal and it is not affected by the neutralization current. For the NIF conditions, the ejection time is equal to the laser pulse duration (1 ns) and it is greater than the neutralization time by a factor of 10: The target charging is strongly limited by the neutralization as well as the EMP strength. That is why the EMP problem is most acute for the laser facilities, which gather a high energy and a short pulse duration.

The holder effect can be included in the model for the cases where the ejection time is much greater than the neutralization time. It prevents the apparition of the surfacic charge and of the associated electrostatic potential. In the case $t_n \ll t_{ej}$, this effect is accounted for by simply removing the electrostatic part of potential barrier. It becomes then:

$$\Delta\Phi(t) = \phi_{th}(t,0) - \phi_{th}(t,x_{min}). \tag{33}$$

For cases where the ejection time and neutralization time are comparable, the model has to be completed with the equation that links the electrostatic potential of the target to the neutralization current:

$$U = Ri_n - L\partial_t i_n, \tag{34}$$

where R and L are the resistivity and inductance characterizing the impedance of the holder and i_n the neutralization current. The tension U takes place of the electrostatic part of the potential barrier:

$$\Delta\Phi(t) = U + \phi_{th}(t,0) - \phi_{th}(t,x_{min}). \tag{35}$$

Equation (34) is highly dependent on the experimental setup and its analysis is out of the scope of the present paper. But a simple example can be provided. In the experiment [8], a capacitor-coil target generates a very high magnetic field: 500 T within a millimetric volume during 1 ns. The target is composed of two disks linked by a small spire and is insulated from the ground. The laser ejects electrons from one disk, which are collected on the other one. The neutralization current goes into the spire and generates the magnetic field. In this example, the laser pulse duration is longer than the characteristic time of the neutralization current. It means that the target is neutralized during the electron ejection. Canceling the electrostatic part of the potential, and using the laser parameters $E_{las} = 200$ J, $t_{las} = 1$ ns, $\lambda_{las} = 1024$ nm, $r_{las} = 20\ \mu$m, and $\eta_{las} = 40\%$, we find a target charge of 60 μC, which is ejected in 1 ns. As the ejection current corresponds to the neutralization current of the same magnitude of 60 kA, the spire of a 250 μm radius produces a magnetic field of 150 T. Note that this rough estimate does not include all physical mechanisms at play in the production of such a high magnetic field.

VI. CONCLUSION

We developed a simple model allowing us to estimate the charging current and the total charge produced on the target by the escaped hot electrons in a high-power laser-target interaction. The model agrees with existing experimental data and provides understanding of the major physical processes. The simple code allows a rapid evaluation of the target charge knowing target and laser parameters. It is described in Appendix E and in the Supplemental Material [22].

Further developments of the model are possible. The spectrum of ejected electrons can be extracted from the model. One can also calculate the electromagnetic emission due to the

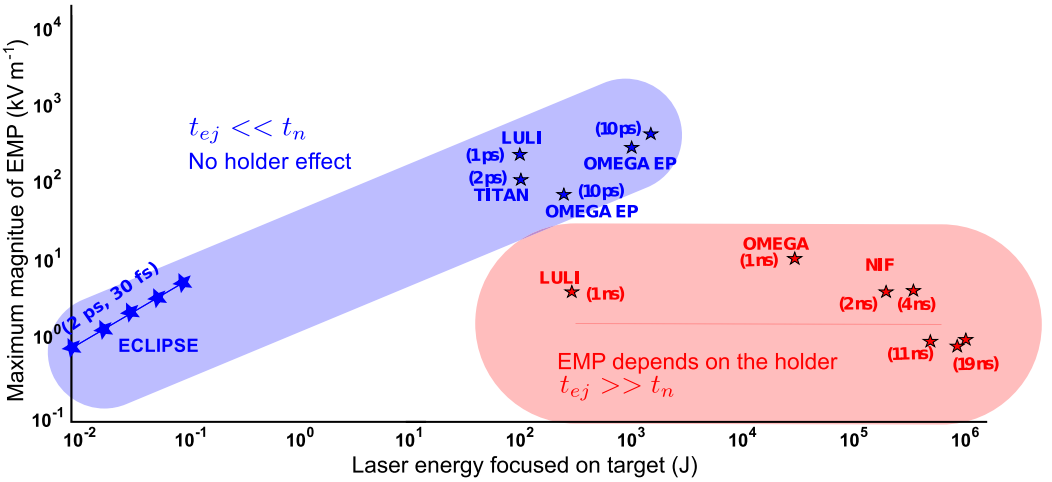

FIG. 17. (Color online) Amplitude of the EMP electric field at 50 cm of the target from various laser facilities versus the laser energy. Blue zone (left) shows the EMP induced by the target charging. Red zone (right) shows the EMP damped by the neutralization.

ejection current,which is typically in the THz frequency range. The model can be also adapted to thin targets.

The global conclusion on this target charging mechanism is its robustness. Many variables are coupled and many physical effects intervene. Nevertheless,a relatively simple model accounting for the hot electron relaxation and the surface electrostatic potential provides reasonable estimates for practically interesting conditions and opens ways for mitigation strategies.

ACKNOWLEDGMENTS

This work was performed within the EUROfusion Consortium and has received funding from the EU's Horizon 2020 research and innovation program, Grant No. 633053. The support from the French National Agency of Research, Projects No. ANR-12-BS04-0006-04 and No. ANR-10-IDEX-03-02, is also acknowledged.

APPENDIX A: COLLISIONS

The collision model is based on the paper by K. Kanaya and S. Okayama [21], which describes the slowdown of an electron inside a solid target. The model calculates the averaged penetration depth, the energy, and the momentum deposition after one, two, or three collisions of the beam electrons with the electrons and the ions of the target according to the collisions probabilities, see Fig. 18. This model originally developed for a monoenergetic electron beam is generalized here by taking an average over the electron energy distribution (1). The characteristic collision times are obtained as follows. First, we set the scattering radius of a hot electron of energy ε according to Ref. [21]:

$$R_m = \frac{2.76\times10^{-11}\varepsilon^{5/3}}{\rho Z^{8/9}}\frac{(1+\varepsilon 0.978\times10^{-6})^{5/3}}{(1+\varepsilon 1.957\times10^{-6})^{4/3}}, \quad \text{(A1)}$$

with ρ being the target density in g/cm^3, A the target mass number, Z the target atomic number, and ε the hot electron energy expressed in eV. The hot-cold electron collision time is obtained as a ratio of the averaged scattering radius by the averaged hot electron speed:

$$t_{ee} = \frac{\langle R_m\rangle}{\langle v\rangle}. \quad \text{(A2)}$$

The hot electron-ion collision time is obtained by adding a weight coefficient to t_{ee}:

$$t_{ei} = \frac{t_{ee}}{1+g}, \quad \text{(A3)}$$

with the factor $g = 0.187\,Z^{2/3}$ which accounts for the electron ion collision ratio. The cooling time is defined as the time interval needed for the temperature to decrease from T_0 to 0.01 T_0:

$$t_{\rm cool} = \int_{0.01\,T_0}^{T_0}\frac{t_{ee}}{T}dT. \quad \text{(A4)}$$

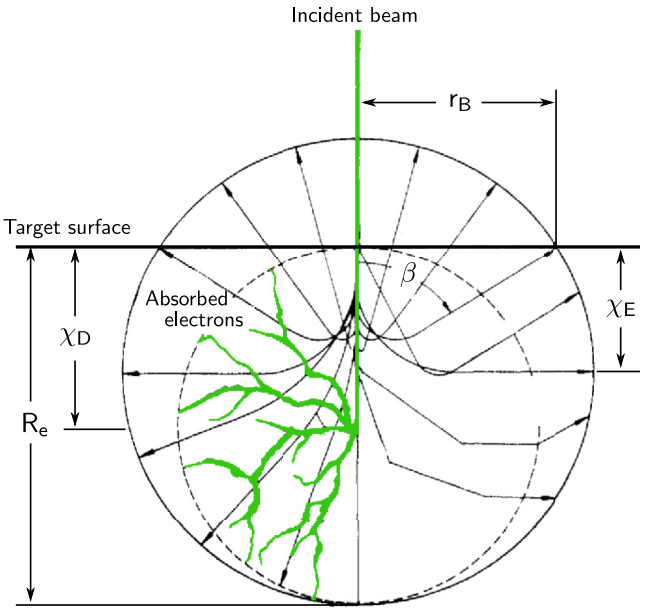

FIG. 18. (Color online) Modified diffusion model of electron beam penetration in a target: R_m is the maximum range, χ_D the penetration depth, χ_E the maximum energy dissipation depth, and r_B the backscattering range. Figure extracted from Ref. [21] with permission.

The electron ejection angle is expressed as a solid angle ratio with half angle β:

$$\Omega_\beta = \sin^2(\beta/2)$$
$$\beta = \arctan\frac{2.2g(1+g)}{1+2g-0.21g^2}. \quad \text{(A5)}$$

APPENDIX B: HOT ELECTRON DENSITY PROFILE

We detail here the calculation of the density profile of the hot electron cloud. In the major part of the electron cloud, the hot electron density is assumed to be homogeneous with its value $n_h = \frac{N_h}{V_h}$. This assumption is insufficient at the target surface where the charge separation generates the thermal potential $\phi_{\rm th}$. The problem is in one dimension along the laser axis ξ. We solve the Poisson equation (19) assuming the Boltzmann distribution of electrons in the potential well:

$$\epsilon_0\partial_\xi^2\phi_{\rm th} = -e[n_i - n_h\exp(e\phi_{\rm th}/k_BT_h)], \quad (19)$$

where ϵ_0 is the vacuum dielectric permittivity. The ion density is described by a Heaviside function, $n_i = (N_h/V_h)\mathcal{H}(-\xi)$, where $\xi = 0$ defines the target surface. Equation (19) is simplified by applying the following normalization: $\hat\phi = e\phi_{\rm th}/k_BT_h$ and $\hat\xi = \xi/\lambda_{\rm Dh}$. The $\hat\xi$ derivations are noted with $'$. One obtains:

$$\hat\phi'' = \exp\hat\phi \quad \text{if } \hat\xi > 0, \quad \text{(B1a)}$$
$$\hat\phi'' = \exp\hat\phi - 1 \quad \text{if } \hat\xi < 0. \quad \text{(B1b)}$$

The boundary conditions for this 1D problem along axial direction are $\hat\phi'(\infty)\to 0$, which corresponds to the absence of the electric field far away in front of the target, and $\hat\phi(\infty)\to-\infty$ and $\hat\phi(-\infty)\to 0$ are imposed by the plasma neutrality far inside the target. We assume also the continuity of the solution at $\hat\xi = 0$. This equation has a divergent solution for the potential in one dimension [17], but a solution for the electron density is convergent.

Equations (B1) are integrated with a multiplication by $\hat\phi'$ on both sides. Then we obtain:

$$\tfrac{1}{2}\hat\phi'^2 = \exp\hat\phi + C_1 \quad \text{if } \hat\xi > 0, \quad \text{(B2a)}$$
$$\tfrac{1}{2}\hat\phi'^2 = \exp\hat\phi - \hat\phi + C_2 \quad \text{if } \hat\xi < 0. \quad \text{(B2b)}$$

We apply the boundary conditions to find that $C_1 = 0$ and $C_2 = -1$. Equating Eqs. (B2a) and (B2b) we obtain the solution at the surface: $\hat\phi(0) = -1$. Then Eq. (B2a) is rewritten. We introduce the function $\hat\chi = \hat\phi + 1$, which is zero at $\hat\xi = 0$, in Eq. (B2b). This equation is linearized using the Taylor development near $\xi = 0$. Note the minus sign in (B3b) is chosen to satisfy the convergence and the sign conventions:

$$\hat\phi'^2 = 2\exp\hat\phi \quad \text{if } \hat\xi > 0, \quad \text{(B3a)}$$
$$\hat\chi' = -\sqrt{2/\exp(1)}\left[1 - \frac{1-\exp(1)}{2}\hat\chi\right] \quad \text{if } \hat\xi < 0. \quad \text{(B3b)}$$

We integrate one more time and use the continuity condition $\hat\phi(0) = -1$ to find the integration constants. The equation (B3a) has several solutions, but only the following one satisfies the convergence and the sign conventions:

$$\hat\phi = -2\ln[\exp(1/2) + \hat\xi/\sqrt{2}] \quad \text{if } \hat\xi > 0, \quad \text{(B4a)}$$
$$\hat\phi = -1 + \frac{2}{1+\exp(1)}[1-\exp(\kappa\hat\xi)] \quad \text{if } \hat\xi < 0. \quad \text{(B4b)}$$

We note $\kappa = \frac{\exp(1)-1}{\sqrt{2}\exp(1)}$. The inside solution, Eq. (B4b), is only valid close to the surface. Because of its divergence, Eq. (B4a) is also valid only close to the surface. In that sense, this solution is not straightforwardly applicable, but it can be used to determine the electron density which is close to the surface.

$$n_e(\xi) = \frac{N_h}{V_h}[\exp(1/2) + \xi/\lambda_{\rm Dh}\sqrt{2}]^{-2} \quad \text{if } \xi > 0, \quad \text{(B5a)}$$
$$n_e(\xi) = \frac{N_h}{V_h}\{1 + [\exp(-1) - 1]\exp(\kappa\xi/\lambda_{\rm Dh})\} \quad \text{if } \xi < 0. \quad \text{(B5b)}$$

APPENDIX C: THERMAL POTENTIAL CALCULATION

The reconstruction of the thermal potential is based on the electron density profile. We demonstrate here that we can find a solution using a 3D calculation and avoiding the divergence of the 1D solution of $\phi_{\rm th}$. We start with the simplification of Eq. (21). Keeping the 1D hypothesis for the charge distribution, we can describe the whole volume by successive $d\xi$ thickness disks at a position ξ with a surface charge $\sigma_e(\xi) = e[n_i(\xi) - n_e(\xi)]d\xi$. Each of those disks generates a potential at the position x along the laser axis:

$$d\phi_{\rm th}(\xi,x) = \frac{\sigma_e(\xi)d\xi}{2\epsilon_0}\left[\sqrt{{R_h}^2 + (\xi-x)^2} - |\xi - x|\right]. \quad \text{(C1)}$$

Then, for a given position x, we integrate the contributions coming from each position ξ with the surface density $\sigma_e(\xi)$. It is written as follows:

$$\phi_{\rm th}(x) = \int_{-\infty}^{\infty}\frac{\sigma_e(\xi)d\xi}{2\epsilon_0}\left[\sqrt{{R_h}^2 + (\xi-x)^2} - |\xi - x|\right]. \quad \text{(C2)}$$

For the contribution inside the target, we simplify the integration assuming that the whole charge density is at $\xi = 0$. The surface charge is then obtained by the integration of Eq. (B5a) to conserve the electroneutrality. One obtains:

$$\sigma_{\rm in} = \frac{eN_h}{V_h}\int_0^\infty d\xi[\exp(1/2) + \xi/\lambda_{\rm Dh}\sqrt{2}]^{-2}$$
$$= \frac{eN_h\lambda_{\rm Dh}}{V_h}\sqrt{\frac{2}{\exp(1)}}, \quad \text{(C3)}$$

$$\phi_{\rm th}(x) = -\int_0^\infty \frac{eN_h\left[\sqrt{{R_h}^2 + (\xi-x)^2} - |\xi-x|\right]}{2\epsilon_0 V_h[\exp(1/2) + \xi/\lambda_{\rm Dh}\sqrt{2}]^2}d\xi$$
$$+ \frac{\sigma_{\rm in}}{2\epsilon_0}\left(\sqrt{{R_h}^2 + x^2} - |x|\right). \quad \text{(C4)}$$

The first step is a rearrangement, gathering the absolute valued variable and the other ones. We also introduce the

same normalization as in Appendix B and the notations $z = x/R_h$, $\lambda = \sqrt{2\exp(1)}\lambda_{\mathrm{Dh}}/R_h$, and $\zeta = \xi/R_h$. Then the potential reads:

$$\hat{\phi}_{\mathrm{th}}(z) = \hat{\phi}_1(z) + \hat{\phi}_2(z), \tag{C5a}$$

$$\hat{\phi}_1(z) = \frac{1}{\lambda}\sqrt{1+z^2} - \int_0^\infty \frac{d\zeta}{(\zeta+\lambda)^2}\sqrt{1+(\zeta-z)^2}, \tag{C5b}$$

$$\hat{\phi}_2(z) = -\frac{|z|}{\lambda} + \int_0^\infty \frac{d\zeta}{(\zeta+\lambda)^2}|\zeta - z|. \tag{C5c}$$

We start with $\hat{\phi}_1$. The integral in (C5b) has a general solution:

$$\begin{aligned}\hat{\phi}_1(z) = \frac{\sqrt{1+z^2}}{\lambda} - \Bigg\{ & \frac{\lambda+z}{\sqrt{(z+\lambda)^2+1}} \ln[\sqrt{1+(\zeta-z)^2} \\ & \times \sqrt{(z+\lambda)^2+1} + 1 + (z+\lambda)(\zeta - z)] \\ & - \frac{(\lambda+z)\ln(\lambda+\zeta)}{\sqrt{(z+\lambda)^2+1}} - \frac{\sqrt{(z-\zeta)^2+1}}{\lambda+\zeta} \\ & - \sinh^{-1}(z-\zeta)\Bigg\}_0^\infty .\end{aligned} \tag{C6}$$

This results in a function of z and a diverging part:

$$\begin{aligned}\hat{\phi}_1(z) = & \frac{\lambda+z}{\sqrt{(z+\lambda)^2+1}} \\ & \times \ln \frac{\sqrt{(z+\lambda)^2+1}\sqrt{z^2+1} + 1 + z(z+\lambda)}{[\sqrt{(z+\lambda)^2+1} - z - \lambda]\lambda} \\ & + 1 - \sinh^{-1}(z) - \sinh^{-1}(\infty).\end{aligned} \tag{C7}$$

The diverging part will be canceled by the other integral $\hat{\phi}_2$. Accounting for the absolute value, the integral can be presented as:

$$\hat{\phi}_2(z) = \frac{z}{\lambda} + \int_0^\infty \frac{\zeta - z}{(\zeta+\lambda)^2} d\zeta \quad \text{if } z < 0. \tag{C8a}$$

$$\begin{aligned}\hat{\phi}_2(z) = & -\frac{z}{\lambda} + \int_0^z \frac{z-\zeta}{(\zeta+\lambda)^2} d\zeta \\ & + \int_z^\infty \frac{-z+\zeta}{(\zeta+\lambda)^2} d\zeta \quad \text{if } z > 0.\end{aligned} \tag{C8b}$$

All the general integrals of (C8) can be calculated explicitly and we obtain:

$$\hat{\phi}_2(z) = -\ln(\lambda) - 1 + \ln(\infty) \quad \text{if } z < 0. \tag{C9a}$$

$$\hat{\phi}_2(z) = -2\ln(\lambda+z) - 1 + \ln(\lambda) + \ln(\infty) \quad \text{if } z > 0. \tag{C9b}$$

While gathering the expressions for $\hat{\phi}_1$ and $\hat{\phi}_2$, the diverging parts compensate each other according to the relation $\sinh^{-1}\infty - \ln\infty = \ln 2$. We finally get the following expression for the thermal potential:

$$\begin{aligned}\tilde{\phi}_{\mathrm{th}}(z) = & \frac{\lambda+z}{\sqrt{(z+\lambda)^2+1}} \\ & \times \ln\left[\frac{\sqrt{(z+\lambda)^2+1}\sqrt{z^2+1} + 1 + z(z+\lambda)}{(\sqrt{(z+\lambda)^2+1} - z - \lambda)\lambda}\right] \\ & - \sinh^{-1}(z) - \ln 2 \\ & + \begin{cases} -\ln(\lambda) & \text{if} \quad z < 0 \\ -2\ln(\lambda+z) + \ln(\lambda) & \text{if} \quad z > 0 \end{cases}.\end{aligned} \tag{C10}$$

APPENDIX D: RECHARGE CURRENT IN DIELECTRIC TARGETS

The charge Q accumulated on a dielectric target differs from the neutralization charge Q_n. Here we calculate the ratio between those two quantities after the end of the neutralization process. The charge Q generates a potential difference with the ground, which induces a neutralization current in the holder. This charge is the measured one Q_n. After the end of the neutralization process the charge Q_n is distributed along the holder. Figure 19 presents a scheme of the potential distribution at the equilibrium. As there is no current, we set a relation between tensions:

$$V_1 = V_2 - \int_0^{\theta_z} E_\theta r d\theta, \tag{D1}$$

with $\theta_z = \sin^{-1}(a/\sqrt{a^2+z^2})$ the angle at the holder surface. The potentials V_1 and V_2 are calculated with the mirror charge assumption:

$$V_1 = 0, \tag{D2a}$$

$$V_2 = \frac{Q}{4\pi\epsilon_0}\left[\frac{1}{\sqrt{d^2+(h-z)^2}} - \frac{1}{\sqrt{d^2+(h+z)^2}}\right]. \tag{D2b}$$

The tangential electric field between the holder and the ground as its shape chosen to verify the Poisson equation $\nabla\vec{E} = 0$, with the lineic charge distribution $q_n(z)$:

$$E_\theta = \frac{q_n(z)}{4\pi\epsilon_0}\frac{1}{r\sin\theta}. \tag{D3}$$

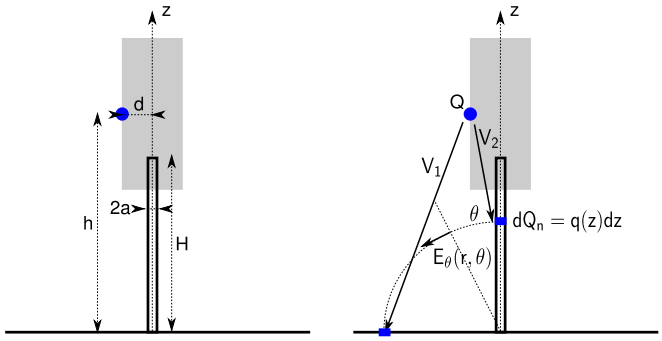

FIG. 19. (Color online) Notation of the distances and a scheme of the potentials among the target, the holder, and the ground at equilibrium.

Combining these three equations, we find the charge distribution $q(z)$ along the holder:

$$q_n = \frac{Q}{2\ln\left(\tan\frac{\theta_z}{2}\right)}\left[\frac{1}{\sqrt{d^2+(h-z)^2}} - \frac{1}{\sqrt{d^2+(h+z)^2}}\right]. \tag{D4}$$

The integration of q_n from 0 to H provides the value of Q_n as a function of geometric parameters and the charge Q. It can be approximated by the following relation:

$$Q_n = \frac{Q}{2\ln(2H/a)}\ln\left\{\frac{(h+\sqrt{d^2+h^2})^2}{[h-H+\sqrt{d^2+(H-h)^2}][h+H+\sqrt{d^2+(H+h)^2}]}\right\}. \tag{D5}$$

In this calculation, there are additional hypothesis. The third-dimension variations are considered as negligible since $H \ll d$. Also the relative dielectric constant of the target is assumed close enough to 1.

The ratio Q_n/Q depends strongly on the position of the laser spot with respect to the holder. A numerical simulation, using the setup described in Ref. [6], of the neutralization current with and without insulating between the charge Q position and the edge of the holder has benchmarked the calculation. The results are presented in Fig. 20. The integration of neutralization current confirms the calculated ratio: One finds $Q_n/Q = 0.28$ from the simulation and 0.22 from (D5) (with $H = 43$ mm, $h = 45$ mm, $a = 0.5$ mm, and $d = 1.7$ mm).

APPENDIX E: CODE DESCRIPTION

1. Numerical descriptions

Figure 21 shows the global scheme of the solver [22]. The temporal scheme is a simple Euler's scheme but the different contributions are split to fit the physics evolution. At the first time step, the radius must evolve one time before any use the cloud volume to avoid a null initial value.

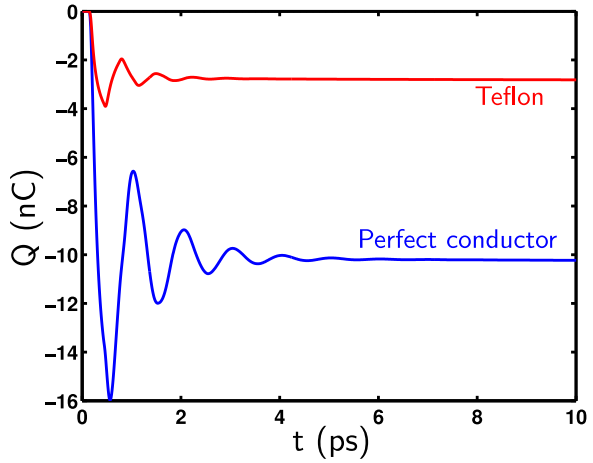

FIG. 20. (Color online) Time dependence of the neutralization charge through the holder with a perfect conductor target and with a Teflon target. Laser parameters: $E_{las} = 80$ mJ, $t_{las} = 50$ fs, and $r_{las} = 4\ \mu$m. Data obtained from numerical simulations with the setup described in Ref. [6].

2. Units and normalizations

Time(ps)	temperature: normalized to $(m_e c^2)$
Length (μm)	number of hot electron: (nC)
Charge (nC)	speed: normalized to (c)
Current (kA)	energy: normalized to $(m_e c^2)$
laser energy (J)	target density: (g/cm^3)

Output units are specified in the output files.

3. User commands

Compilation command: gfortran -O3 -fdefault-real-8 Cho CoLaT.f90

Launch command:./a.out ⟨⟩, where the argument is the four-digit number of the input file.

Input file: Its name is input_0001.txt. The format is txt and ascii and an example is provided in Ref. [22].

4. Code's outputs

The code produces three files named output_scalar_0001.txt, output_fdistr_0001.txt, and output_potent_0001.txt with the number corresponding to the input file one. Each file has the same header gathering the input data plus the initial temperature, the cooling time, the total charge, and the rate of electron accelerated. After this header, the scalar file contains the time evolutions of R_h, λ_{Dh}, T_h, n_h, N_h, $\Delta\Phi$, J, and Q. The potential file contains the time evolutions of $\Delta\Phi$, $\phi_E(0)$, $\phi_E(x_{min})$, $\phi_{th}(x_{min})$, $\phi_{th}(0)$, and x_{min}. The distribution function file contains the time evolutions of $\mathcal{A}$, $\mathcal{A}_{hot}$, $\langle v\rangle$, $\langle v\rangle_{hot}$, $\langle\varepsilon\rangle$, $\langle\varepsilon\rangle_{hot}$.

5. CFL illustration

The code involves a time step dt and an energy discretization $d\varepsilon$. The code is limited by a CFL time versus energy. This CFL is not analytically defined but explored numerically in Fig. 22(a). We also provide in Fig. 22(b) the typical shapes of the current associated with the typical troubles. The green one is the reference. The dashed red curve presents a default at $t = 0.04$ ps: The time step is too big and the first time step charge generates an overestimated electrostatic potential, which strongly damps the current on the second time step. This default does not change the integration value but can make the resolution unstable.

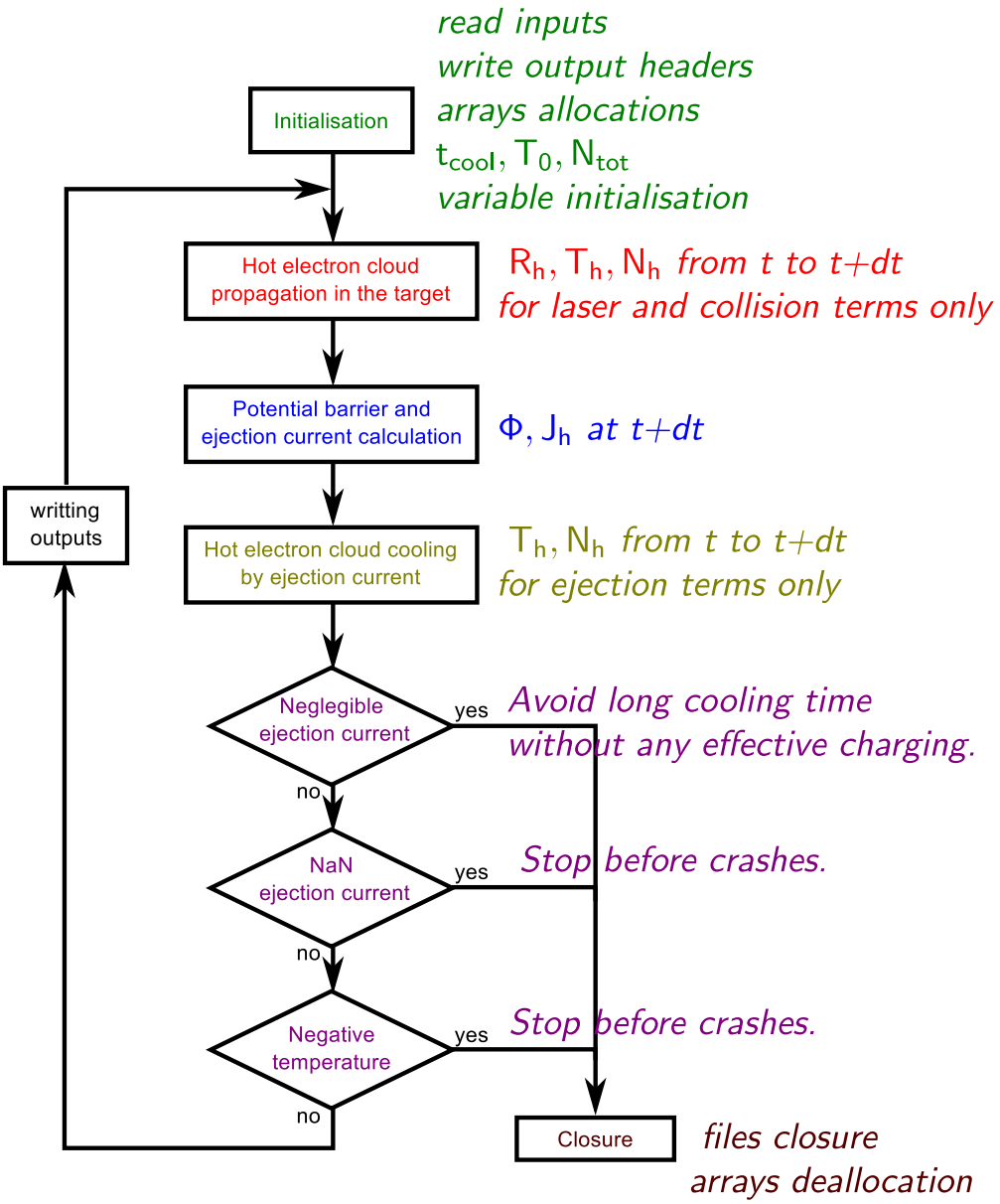

FIG. 21. (Color online) Schematic process of the equation solver.

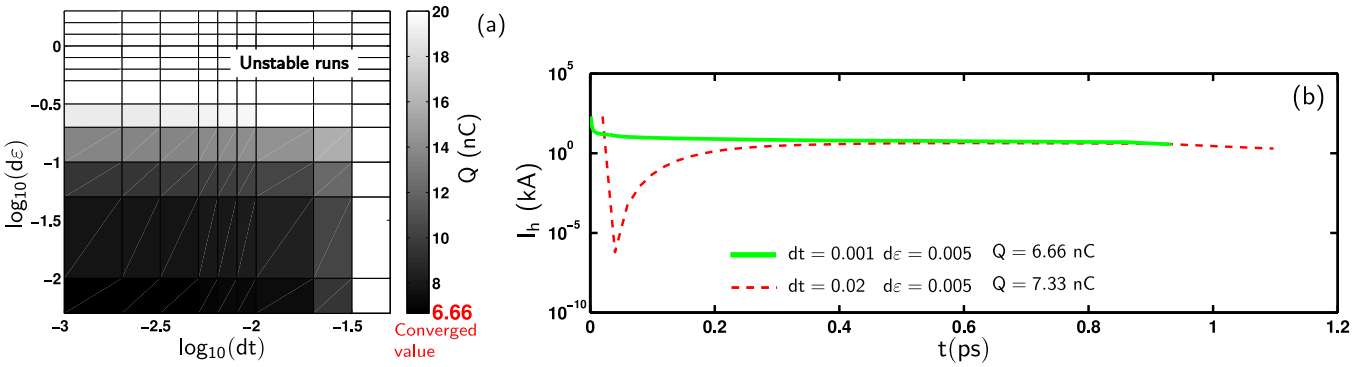

FIG. 22. (Color online) (a) Final charge obtained for various values of dt and $d\varepsilon$. The converged result equals 3.40 nC. (b) Temporal evolution of the current for different resolutions: $E_{las} = 0.08$ J, $r_{las} = 6$ um, $\lambda_{las} = 800$ nm, $t_{las} = 0.5$ um, and $\eta_{las} = 40\%$.

[1] J. S. Pearlman *et al.*, Appl. Phys. Lett. **31**, 414 (1977).
[2] M. J. Mead *et al.*, Rev. Sci. Instrum. **75**, 4225 (2004).
[3] C. G. Brown Jr. *et al.*, J. Phys. Conf. Ser. **112**, 032025 (2008).
[4] A. Sagisaka *et al.*, Appl. Phys. B **90**, 373 (2008).
[5] J. E. Bateman *et al.*, RAL Technical Reports, RAL-TR-2012-005 (2012).
[6] J.-L. Dubois *et al.*, Phys. Rev. E **89**, 013102 (2014).
[7] S. Fujioka *et al.*, Sci. Rep. **3**, 1170 (2013).
[8] J. J. Santos *et al.*, New J. Phys. **17**, 083051 (2015).
[9] A. Poye *et al.*, Phys. Rev. E **91**, 043106 (2015).
[10] P. Gibbon, *Short Pulse Laser Interaction with Matter, an Introduction* (World Scientific, London, 2005).
[11] F. N. Beg *et al.*, Phys. Plasmas **4**, 447 (1997).
[12] S. C. Wilks, W. L. Kruer, M. Tabak, and A. B. Langdon, Phys. Rev. Lett. **69**, 1383 (1992).
[13] R. Fabbro *et al.*, Phys. Fluids **28**, 1463 (1985).
[14] J. E. Crow, J. Plasma Phys. **14**, 65 (1975).
[15] P. Mora, Phys. Rev. Lett. **90**, 185002 (2003).
[16] M. Passoni and M. Lontano, Phys. Rev. Lett. **101**, 115001 (2008).
[17] N. J. Carron *et al.*, IEEE Trans. Nucl. Sci. **23**, 1986 (1976).
[18] D. C. Eder *et al.*, Lawrence Livermore National Laboratory Report, LLNL-TR-411183 (2009).
[19] Z. Y. Chen *et al.*, Phys. Plasmas **19**, 113116 (2012).
[20] K. Quinn *et al.*, Phys. Rev. Lett. **102**, 194801 (2009).
[21] K. Kanaya and S. Okayama, J. Phys. D: Appl. Phys. **5**, 43 (1972).
[22] See Supplemental Material at http://link.aps.org/supplemental/10.1103/PhysRevE.92.043107 for FORTRAN90 source code and its input file.